1   **The MEMIC: An *ex vivo* system to model the complexity of the tumor**

2   **microenvironment**

3   Libuše Janská, Libi Anandi, Nell C. Kirchberger, Zoran S. Marinkovic, Logan T.

4   Schachtner, Gizem Guzelsoy, Carlos Carmona-Fontaine*

5   Center for Genomics & Systems Biology, Department of Biology, New York University,

6   New York, NY 10003, USA

7   *e-mail for correspondence: cf97@nyu.edu

8 **ABSTRACT**

9 There is an urgent need for accurate, scalable, and cost-efficient models of the

10 complexity and heterogeneity of the tumor microenvironment. Here, we detail how to

11 fabricate and use the Metabolic Microenvironment Chamber (MEMIC) – a 3D-printed *ex*

12 *vivo* model of intratumoral heterogeneity. A major driver of the cellular and molecular

13 diversity in tumors is the accessibility to the blood stream that provides key resources

14 such as oxygen and nutrients. While some tumor cells have direct access to these

15 resources, many others must survive under progressively more ischemic environments

16 as they reside further from the vasculature. The MEMIC is designed to simulate the

17 differential access to nutrients and allows co-culturing different cell types, such as tumor

18 and immune cells. This system is optimized for live imaging and other microscopy-

19 based approaches and it is a powerful tool to study tumor features such as the effect of

20 nutrient scarcity on tumor-stroma interactions. Due to its adaptable design and full

21 experimental control, the MEMIC can provide novel insights into the tumor

22 microenvironment that would be difficult to obtain via other methods. As a proof of

23 principle, we show that cells can sense gradual changes in metabolite concentration,

24 and tune intracellular cell signaling to form multicellular spatial patterns of cell

25 proliferation. We also show that ischemic macrophages reduce epithelial features in

26 neighboring tumor cells highlighting the power of this system to study cell-cell

27 interactions and non-cell autonomous effects of the metabolic microenvironment. We

28 propose that the MEMIC can be easily adapted to study early development, ischemic

29 stroke, and other systems where multiple cell types interact within heterogeneous

30 environments.

31 **INTRODUCTION**

32 The tumor microenvironment is a complex cellular ecosystem (Fig. 1A). This complexity

33 includes a large diversity of malignant and non-malignant cells such as fibroblasts and

34 immune cells (Junttila and Sauvage, 2013; Merlo et al., 2006; Tabassum and Polyak,

35 2015). These cells secrete and consume molecular signals, growth factors, and

36 metabolites, creating an intricate biochemical landscape in the tumor interstice that in

37 turn affects tumor cell behaviors and cell-cell interactions (Bader et al., 2020; Buck et

38 al., 2017; Mehta et al., 2017; Wiseman and Halliwell, 1996).

39 We and others have shown how insufficient tumor vascularization can produce

40 predictable spatial patterns of cell phenotypes (Carmona-Fontaine et al., 2017b). Cells

41 located near functional blood vessels are constantly perfused with nutrients and oxygen.

42 In contrast, cells distant from vasculature, or proximal to faulty vessels commonly found

43 in solid tumors (Mazzone et al., 2009), are in a microenvironment poor in nutrients and

44 profuse in potentially toxic metabolic waste products (Carmeliet and Jain, 2000a;

45 Gatenby and Gillies, 2004; Hobson-Gutierrez and Carmona-Fontaine, 2018a;

46 Thomlinson, 1977a). The role that nutrients and other metabolites have in modulating

47 the behavior and phenotypes of tumor – and especially immune cells – has been the

48 subject of recent interest (Buck et al., 2017; Hobson-Gutierrez and Carmona-Fontaine,

49 2018a; Olenchock et al., 2017a; Pavlova and Thompson, 2016a). However, the lack of

50 amenable models of the metabolic microenvironment of tumors hampers the ability to

51 predict and control the effect of environmental metabolites on tumor cells.

52 Animal models are a fundamental tool to study the complex and heterogeneous tumor

3

53   microenvironment (Day et al., 2015; Gould et al., 2015). However, the complexity of

54   animal physiology – while crucial in pre-clinical studies – can challenge the isolation of

55   individual experimental variables, and their use for large experiments is severely limited

56   by practical, economical, and ethical concerns (Bert et al., 2017; Bressers et al., 2019).

57   On the other side of the spectrum, conventional *in vitro* experiments offer much better

58   experimental control and can be easily used in high throughput approaches. However,

59   these cultures do not model the metabolic heterogeneity and other essential features of

60   the tumor microenvironment. The recent resurgence in the use of three-dimensional

61   tumor organoids – or *tumoroids* – as a tool to model different aspects of tumor biology

62   does offer some of these features (Clevers, 2016). Tumoroids can recapitulate key

63   histopathological tumor characteristics, and they can be used to screen for patient-

64   specific drug responses (Boj et al., 2015; Gao et al., 2014; van de Wetering et al.,

65   2015). However, the organization of tumoroids emerges spontaneously and thus the

66   visualization, quantification, and prediction of their organization remains challenging

67   (Fig. 1B).

68   We previously developed a microphysiological system that mimics the complexity of the

69   tumor microenvironment in a well-controlled and predictable manner. This Metabolic

70   Microenvironment Chamber (MEMIC) is suitable for high resolution microscopy

71   analyses and can be easily adapted to the complexity and throughput that different

72   experimental scenarios may need (Carmona-Fontaine et al., 2017b). Cells in the

73   MEMIC are gradually limited in their access to fresh media, generating gradients of

74   extracellular metabolites and oxygen across the chamber where they are cultured. This

75   metabolic heterogeneity can be accompanied by the addition of other components of

76   the tumor microenvironment, such as stromal cells, an extracellular matrix, and

77   perturbations with carcinogens or drugs. Compared to the methods mentioned above,

78   the spatiotemporal complexity that emerges in the MEMIC is predictable, reproducible,

79   and measurable.

80   Here, we expand on key features of the MEMIC and provide detailed guidelines on how

81   to use this system. We determined key parameters that shape metabolic gradients in

82   the MEMIC, which we describe alongside detailed information on how to assemble the

83   platform, how to set up cultures of tumor cells – alone or in co-culture – and how to

84   monitor these experiments using live imaging and fixed endpoint microscopy assays,

85   such as immunofluorescence. We demonstrate that the MEMIC accurately captures the

86   cellular response to nutrient and oxygen deprivation that occur *in vivo,* and we show

87   that nutrient-deprived macrophages reduce epithelial features in neighboring tumor

88   cells. Finally, we provide an image analysis pipeline designed to obtain information at

89   the single-cell level from MEMIC images suitable for users without any coding

90   experience. We propose the MEMIC as a complement to standard *in vitro* and *in vivo*

91   experiments, diversifying the tools available to accurately model, perturb, and monitor

92   the tumor microenvironment, as well as to understand how extracellular metabolites

93   affect other processes such as wound healing and stem cell differentiation.

94 **RESULTS**

95 **MEMIC – an overview**

96 A hallmark of the microenvironment of virtually all solid tumors is the presence of

97 hypoxic and poorly nourished niches (Gatenby and Gillies, 2008; Hobson-Gutierrez and

98 Carmona-Fontaine, 2018b; Lyssiotis and Kimmelman, 2017; Thomlinson, 1977b).

99 These conditions are the result of the increased growth of tumor cells and insufficient

100 blood perfusion (Baish and Jain, 2000; Carmeliet and Jain, 2000b; Pavlova and

101 Thompson, 2016b). Because tumor growth and tumor vascularization are not uniform,

102 they create a heterogeneous 'metabolic microenvironment' where some cells

103 experience near physiological conditions, whereas others endure severe ischemia, and

104 potentially cell death, due to lack of nutrients and accumulation of toxic waste

105 (Carmona-Fontaine et al., 2013; Gatenby and Gillies, 2008; Thomlinson, 1977b). The

106 MEMIC is a 3D-printed microphysiological culture system specifically designed to model

107 this spectrum of metabolic conditions (Video 1). In addition, the MEMIC allows co-

108 culturing any number of cell types to study how different cells interact and behave in

109 different metabolic niches (Carmona-Fontaine et al., 2017b).

110 To generate these gradients of metabolic conditions, cells in the MEMIC grow inside a

111 small chamber that is connected – only from one end – to a large reservoir of fresh

112 media (or outer chamber, Fig 2A,B). The concentration gradients of extracellular

113 metabolites in the MEMIC are established by a balance between their diffusion rate and

114 their rates of consumption and secretion by cells in the small chamber. Cells proximal to

115 the opening, therefore, have a constant supply of nutrients and oxygen and the

6

116   metabolic byproducts they secrete are quickly cleared by fresh media from the

117   reservoir. In contrast, cells at the opposite end of the small chamber endure a

118   microenvironment where oxygen and nutrients are scarce and metabolic byproducts

119   accumulate (Fig 2C).

120   The MEMIC framework described here is composed of 12 independent MEMIC

121   chambers facilitating multiplexing, technical replicates, and no-gradient controls (Fig

122   2A). The small chamber where cells grow is sealed by optical glass coverslips, and thus

123   it is ideal for high resolution microscopy analyses (Fig 2B). The 12-MEMIC framework

124   has the same footprint as a multi-titer plate and is therefore compatible with

125   conventional equipment such as microscope stages. The main requirement to fabricate

126   a MEMIC is access to a 3D printer, which is inexpensive when compared to most lab

127   equipment, and they are often available as a shared resource at universities and

128   research institutions. In the Supplementary Information linked to this article, we provide

129   a detailed protocol and a video on how to 3D print and assemble this system (Fig S1,

130   Video 2, SI Fabrication).

131   **Cellular responses to nutrients and oxygen gradients**

132   To observe the cellular responses to metabolic gradients, we quantified the activation of

133   key nutrient and oxygen sensing pathways. The mammalian target of rapamycin

134   (mTOR) pathway is a major nutrient sensor and a regulator of anabolic metabolism

135   (Saxton and Sabatini, 2017). We first cultured human colorectal adenocarcinoma cells

136   (DLD1) in the MEMIC for 24h and we then used immunofluorescence to detect

137   phosphorylated S6 (p-S6) as a read-out of TORC1 pathway activation. For a detailed

7

138 description on how to seed cells in the MEMIC and to process them for

139 immunofluorescence, please refer to the Supplementary Information (Fig S2, SI

140 Seeding and processing). Cells in these cultures, show high levels of S6

141 phosphorylation near the opening of the MEMIC but these levels decrease dramatically

142 under ischemic environments (Fig 2D). Conversely, Hypoxia-inducible factor 1-alpha

143 (HIF1α) is a transcription factor that regulates the cellular response to hypoxia. In the

144 absence of oxygen, HIF1α is stable and accumulates in the nucleus, otherwise it is

145 targeted for proteasomal degradation. HIF1α is barely detectable near the opening of

146 the MEMIC, but its levels steeply increase in ischemic regions (Fig 2D). A similar

147 decrease in activation of the mTOR pathway (Palm et al., 2015) and increase of HIF1α

148 (Zhong et al., 1999) has been observed in solid tumors *in vivo*.

149 To acquire information at the single-cell level, we wrote software that rapidly detects cell

150 nuclei, segments individual cells and obtains key parameters such as their position,

151 area, and fluorescence intensity (Fig 2E). This approach is similar to flow cytometry in

152 that it quantifies the fluorescence of individual cells, but unlike flow cytometry, it retains

153 critical spatial information. To help the wider research community use this image

154 cytometry approach, we provide MATLAB scripts and a step-by-step tutorial fit for

155 scientists without any coding experience (see Image cytometry section in

156 Supplementary Information).

157 We used this image cytometry approach to analyze the images shown in Fig 2D. We

158 first plotted HIF1α level for every cell *versus* its p-S6 levels (Fig 2F). To incorporate

159 spatial information, we color-coded each cell on the plot according to its distance from

8

160   the MEMIC opening. To emphasize the role of positional information and the spatial

161   patterns that emerge we can plot the fluorescence levels of each cell *versus* its distance

162   from the opening of the MEMIC as shown in Fig 2G. The quantification shows an

163   exponential decrease in mTOR activation as cells are further away from the opening –

164   consistent with a gradual decrease in nutrient availability. By contrast, we observed a

165   sharp increase in nuclear HIF1α within ischemic areas of the MEMIC. Although oxygen

166   levels are expected to form a smooth gradient, we observe a stepwise increase in

167   HIF1α levels. This digital response emerges from the threshold of oxygen tension that

168   determines whether HIF1α is degraded or not (Lee et al., 2015; Wong et al., 2011).

169   Overall, these results illustrate the formation of metabolite concentration gradients in the

170   MEMIC and show that these gradients are translated into finely tuned intracellular

171   signaling pathways.

172   **Shaping metabolic gradients in the MEMIC**

173   Interstitial levels of extracellular metabolites *in vivo* are determined by a balance of

174   metabolite diffusion and cellular activities such as consumption and secretion rates. As

175   such, the slopes of concentration gradients of these metabolites vary according to

176   tissue crowding, nutrient transporter levels, growth rate, and other parameters that are

177   difficult, or impossible, to untangle *in vivo*. Gradients in the MEMIC are formed by the

178   same principles, however, in this system we are able to tune parameters independently

179   and shape these gradients according to specific experimental needs.

180   To accurately measure and tune parameters in the MEMIC, we used a fluorescent

181   hypoxia reporter as a readout for metabolic gradients ((Vordermark et al., 2001) see SI

9

182   for details). We engineered human breast tumor cells (MDA-MB-231) to express GFP

183   under the control of five HIF1α binding sites (Fig 3A). As a fluorescence reference, we

184   also expressed a membrane-bound form of mCherry in these cells (mCherry-CAAX, see

185   SI for details).

186   Denser cultures should form steeper gradients as more cells consume nutrients and

187   oxygen. To test the effect of cell density on these gradients, we seeded different cell

188   numbers into the MEMIC and measured GFP levels after 24 hours. With the lowest cell

189   density (125 cells/μL or ~12% confluency), GFP signal was not detectable, indicating

190   that the collective oxygen consumption was not enough to activate a hypoxic response

191   even in the far end of the chamber (Fig 3B). At higher cell densities, however, GFP

192   signal becomes evident and its intensity gradients are steeper, have a larger amplitude,

193   and peak closer to the opening. At the highest cell density (1000 cells/μL or >100%

194   confluency) GFP levels peak almost at the opening of the MEMIC (Fig 3B). From there,

195   GFP levels drop as cells become anoxic and necrotic (Fig 3B). Together, these results

196   confirm that denser cultures produce steeper metabolic gradients. In subsequent

197   experiments, we used intermediate cell densities (250-500 cells/μL) that create strong

198   gradients but that are shallow enough to clearly distinguish well-nurtured, nutrient-

199   deprived, and necrotic regions within the MEMIC (e.g. Fig 2C).

200   The formation of the ischemic gradient is a dynamic process. To establish how these

201   gradients develop over time, we seeded the same engineered MDA-MB-231 cells into

202   the MEMIC and tracked their fluorescence levels using live microscopy and image

203   analysis. While constitutive membrane-mCherry levels remain constant (Video 3), GFP

10

204   levels dramatically increase after about 12h in the distal regions of the MEMIC (Fig 3C,

205   Video 3). Over time, the amplitude of the gradient increases and it becomes steeper. In

206   a control culture where cells were well-nurtured throughout the well, no hypoxia was

207   detectable throughout the entire experiment (Fig 3C).

208   We expected that the intensity and shape of metabolic gradients will also depend on the

209   geometry of the MEMIC chamber. Using mathematical modeling we predicted that the

210   height of the MEMIC is the critical geometric parameter in determining the position and

211   slope of metabolic gradients (Carmona-Fontaine et al., 2013). This model also predicts

212   that the width of the MEMIC's opening should not affect the shape of the gradient. To

213   test these predictions, we seeded a constant number of MDA-MB-231 cells expressing

214   the 5xHRE/GFP hypoxia reporter in MEMICs with different heights or with different

215   opening widths and we imaged them after 24 hours ($5x10^5$ cells, Fig. 3D,E). As

216   predicted by our model, changing the width of the opening did not affect the shape of

217   metabolite gradients. Cells seeded in MEMICs with different opening widths increased

218   GFP expression at a constant distance from the opening. When we plot the GFP levels

219   *versus* distance to opening, the signal from all experiments collapse into a single curve

220   regardless of the opening width used (Fig 3D). While the width of the MEMIC opening

221   has little physiological relevance, it has an important experimental implication: the exact

222   position of the top coverslip does not matter as long as the edge of the glass is used as

223   a reference point. This observation makes the fabrication of MEMICs easier and more

224   reproducible.

225   As shown in figure Fig 3E, the height MEMIC chamber is indeed key in shaping

226   ischemic gradients. Cells cultured in thin MEMIC chambers (short height) have less

11

227   media, resulting in steeper gradients that peak close to the opening (Fig 3E). In taller

228   chambers, ischemic gradients are shallower and peak further inside the chamber. The

229   length scales in the MEMIC are much larger than *in vivo* where cells are tightly packed,

230   and thus, their equivalent of the MEMIC height parameter is very small. As a reference

231   point, tumor cells are completely hypoxic at about 150-200μm from the closest blood

232   vessel (Carmona-Fontaine et al., 2017a; Hobson-Gutierrez and Carmona-Fontaine,

233   2018a; Thomlinson, 1977a). This distance is about an order of magnitude smaller than

234   gradients in the MEMIC and spans only about 10-20 cell diameters. The shallower

235   gradients in the MEMIC stretch spatial patterns to a few hundred cell diameters, greatly

236   increasing the spatial resolution of our experiments. Despite this being an advantage for

237   our experiments, it is important to keep in mind these scale differences and adapt the

238   MEMIC's geometry if needed.

239   **Effects of metabolic gradients on cell proliferation**

240   Nutrients provide the biomass and energy that all cells require to proliferate, and tumor

241   cells are no exception. Cells in perivascular, and other well-perfused tumor regions,

242   proliferate actively, while cells within nutrient-deprived tumor regions often show lower

243   growth rates, senescence, and they can ultimately die (Carmona-Fontaine et al., 2013;

244   Gatenby and Gillies, 2008; Thomlinson, 1977b). We wanted to test whether we can

245   reproduce these spatial patterns of cell proliferation in the MEMIC. We used cells

246   expressing FUCCI (Fluorescent Ubiquitination-based Cell Cycle Indicator, Fig 4A), a

247   dual fluorescent reporter that enables the visualization of cell cycle progression

248   (Sakaue-Sawano et al., 2008). Using our image cytometry approach (Fig. 2E), we

12

249 quantified fluorescence levels *per* nuclei. To avoid confounding effects due to

250 aneuploidy and polyploidy that most tumor cells have, we used RPE1 cells – a nearly

251 diploid immortalized epithelial human cell line with a relatively stable genome (Davoli

252 and Lange, 2011; Watkins et al., 2020). RPE1 cells proliferate rapidly, as shown by the

253 many cells in M phase in the no gradients control culture (Fig 4B). The same was true in

254 well-nurtured regions of the MEMIC. However, ischemic cells showed a stark arrest at

255 G_1 denoted by high mKO2-CDT1 and low mAG-GMNN levels (Fig 4C). A similar arrest

256 at G_1 has been reported in tumors *in vivo* (Yano et al., 2014). *De novo* nucleotide

257 synthesis is very sensitive to nutrient limitation (Ducker and Rabinowitz, 2016),

258 suggesting that ischemic cells in the MEMIC – and in tumors– may arrest in G_1 as they

259 fail to synthetize enough nucleotides to duplicate their genomes. We detected a similar

260 spatial pattern of cell proliferation in tumor cells using immunofluorescence. Lung

261 adenocarcinoma cells proliferate rapidly as evidenced by a high number of nuclei

262 positive for phosphorylated Histone H3 (p-H3). As shown in Fig 4D, these numbers

263 decline rapidly in ischemic regions of the MEMIC (Fig 4D, E). Overall, these results

264 show that metabolic gradients in the MEMIC induce changes in cell proliferation that are

265 consistent with nutrient availability and *in vivo* observations. More broadly, these proof-

266 of-principle data show the important role that extracellular metabolites play in producing

267 spatial patterns of cell behavior.

268 **Untangling the effects of different metabolites in the MEMIC**

269 The fast proliferation rate of tumor cells requires exogenous sources of multiple

270 nutrients including glucose (Gatenby and Gillies, 2004; Heiden et al., 2009), aspartate

271 (Birsoy et al., 2015; Sullivan et al., 2015), non-essential amino acids such as glutamine

272 (Son et al., 2013), glycine (Jain et al., 2012), serine (Maddocks et al., 2012; Possemato

273 et al., 2011), and asparagine (Halbrook et al., 2020; Krall et al., 2020; Pavlova et al.,

274 2018), as well as diet-derived essential amino acids, vitamins, and lipids (Bose et al.,

275 2020). Ischemic tumor cells *in vivo* experience reduced levels of oxygen and all these

276 numerous nutrients – and the accumulation of secreted metabolic byproducts such as

277 lactate. Modeling this complex environment is difficult, and thus, most cell metabolism

278 studies focus on limiting a single substrate.

279 In the MEMIC cells spontaneously form complex metabolic gradients, better

280 approximating *in vivo* conditions. While these more physiological conditions can be

281 advantageous, they also can also challenge the experimental uncoupling of individual

282 metabolites and their hierarchical relationships. Here we provide an experimental

283 approach to tackle this challenge. First, in the MEMIC we can easily distinguish effects

284 that *require* hypoxia from changes produced by nutrient scarcity. To do this separation,

285 we take advantage of the gas permeability of polydimethylsiloxane (PDMS (Cox and

286 Dunn, 1986)). PDMS is a biocompatible and transparent polymer that we shape into

287 membranes the size of the conventional glass coverslips that we use in the MEMIC

288 (Fig. S1). Cells in MEMICs sealed with a PDMS membrane – instead of a glass

289 coverslip – will experience gradients of nutrients but no hypoxia as oxygen is rapidly

290 equilibrated across the PDMS membrane (Fig. 5A). To illustrate this approach, we

291 cultured cells expressing the 5xHRE/GFP hypoxia reporter and we grew them in

292 MEMIC constructed with glass, PDMS, or no coverslips (Fig 5A). As shown in Figure 5,

293 only cells in a MEMIC sealed with glass showed GFP signal gradients (Fig 5C). To test

14

294   if hypoxia is *sufficient* to produce a particular effect, these MEMIC experiments can be

295   complemented with conventional *in vitro* cultures in hypoxic incubators where oxygen is

296   set at specific tensions. Similarly, to determine the effects of specific soluble nutrients

297   we can simply remove them from the media formulation, or we can add them at

298   saturating concentrations. For example, we demonstrate that a decrease in media pH-

299   directly induced cell death by increasing the buffer capacity of culture media (Carmona-

300   Fontaine et al., 2013). Overall, this section illustrates that cells in the MEMIC create

301   complex metabolic gradients while still allowing to untangle, identify, and manipulate

302   specific microenvironmental factors.

303   **Ischemic macrophages decrease epithelial features in neighboring tumor cells**

304   The complexity of the microenvironments within the MEMIC can be increased as

305   needed. For instance, we can incorporate additional cell types to approximate the *in*

306   *vivo* microenvironment and to study cell-cell interactions under different metabolic

307   conditions. Extracellular metabolites can directly modulate cell phenotypes and tumor-

308   immune interactions (Buck et al., 2017; Olenchock et al., 2017b).

309   We and others have previously shown that tumor-secreted lactate and low oxygen

310   tension induce a pro-angiogenic phenotype in tumor-associated macrophages

311   (Carmona-Fontaine et al., 2017a; Colegio et al., 2014; Wenes et al., 2016). Here we

312   focused on how ischemic macrophages affect neighboring tumor cells. We first

313   observed that virtually every ischemic tumor cell cultured in the MEMIC became more

314   dysplastic, lose their multicellular epithelial arrangements, and adopt a round or spiked

315   morphology. These effects were exacerbated when tumor cells were co-cultured with

15

316   Bone Marrow-Derived Macrophages (BMDMs). We thus hypothesized that ischemia

317   and the presence of macrophages synergize to alter the morphology of tumor cells.

318   To formally test this idea, we used clones derived from MMTV-PyMT breast tumors. In

319   culture, these cells form geometric epithelial structures and display high levels of E-

320   Cadherin and other epithelial markers (Fig 6A,B). Consistent with the known effects of

321   hypoxia, we observed a significant decrease in E-Cadherin levels in ischemic cells (Fig

322   6A). We compared these results with similar experiments where we co-cultured the

323   same tumor cells with BMDMs, ensuring we maintained the same total cell number. In

324   these co-cultures, ischemic tumor cells dramatically reduced their epithelial morphology

325   and the drop in E-Cadherin was much stronger and it occurred closer to the opening

326   (Fig 6B,C). These morphological and molecular changes suggest that tumor cells are

327   undergoing epithelial to mesenchymal transition (EMT) – a key step in the development

328   of most carcinomas which represent ~80% of all solid tumors, (Weinberg, 2013).

329   Consistent with our observations, HIF1α directly promotes EMT (Dongre and Weinberg,

330   2018; Nieto, 2013) and tumor-associated macrophages can also drive EMT in tumors

331   (Condeelis and Pollard, 2006; Linde et al., 2018). Our results suggest that ischemia and

332   signals from *ischemic* macrophages synergize to trigger EMT in tumor cells (Fig 6D).

333   While the molecular underpinnings of this synergy still need to be elucidated, these

334   results illustrate how the MEMIC can be used to study the interplay between different

335   cellular and molecular factors in the tumor microenvironment.

16

336 **DISCUSSION**

337 *In vivo* animal tumor models are – and will continue to be – crucial in cancer research.

338 However, they are expensive and difficult to scale up. Additionally, it is virtually

339 impossible to accurately control and measure multiple experimental parameters in these

340 experiments. At the other extreme of the experimental spectrum, conventional *in vitro*

341 cell cultures allow the control of most experimental parameters, but this simplicity

342 comes at the cost of losing the context of the intricacy and heterogeneity of tumors. The

343 microphysiological culture system described here – named MEMIC – seeks to bridge

344 these extremes by re-creating key aspects of the complexity of tumors under tunable

345 and controllable conditions.

346 Cells in the MEMIC form concentration gradients of oxygen and nutrients equivalent to

347 those formed in tumors *in vivo*. These different levels of nutrients induce changes in

348 major signaling pathways that in turn change cell behaviors and phenotypes in

349 predictable spatial patterns. As an example, we showed how concentration gradients of

350 nutrients in the MEMIC lead to a heterogeneous microenvironment that ranges from

351 well-nurtured conditions – where cells rapidly proliferate – to increasingly more ischemic

352 environments where cells show cell cycle arrest. This heterogeneous distribution of

353 resources and the resulting regions with high and low cell proliferation are well

354 documented in the analysis of histological tumor samples from patients (Weinberg,

355 2013).

356 The simplicity and affordability of the MEMIC makes it compatible with mid- to high-

357 throughput experiments and screens. Most chemotherapy drugs target rapidly

17

358 proliferating cells, senescent and non-proliferating tumor cells are spared and leading to

359 lower tumor regression and relapse (Gordon and Nelson, 2012; Oshima et al., 2020).

360 Thus the MEMIC could be particularly useful for screening drugs that more efficiently

361 target ischemic regions of tumors, where non-proliferating cells are abundant.

362 Since nutrient levels change gradually with distance from their source, cellular changes

363 in the MEMIC follow predictable spatial patterns. We and others have previously shown

364 that similar spatial patterns emerge *in vivo* following the distribution of the vascular

365 network (Carmona-Fontaine et al., 2017b; Gatenby and Gillies, 2008; Hobson-Gutierrez

366 and Carmona-Fontaine, 2018b; Thomlinson, 1977b). The idea that nutrient and oxygen

367 availability influence cell behavior and the tumor microenvironment is not new.

368 However, this effect has been hard to model experimentally. With the combined power

369 of *in vivo* observation and experiments in the MEMIC, we can argue that metabolite

370 gradients do not only change cell phenotypes, but they organize and pattern the tumor

371 microenvironment.

372 The spatial patterns that nutrient gradients impose in the tumor microenvironment also

373 modulate cell-cell interactions. We showed here that ischemic macrophages reduce

374 epithelial features in neighboring tumor cells. This inhibition of epithelial features is

375 much stronger than the direct effects of nutrient deprivation alone. We thus propose that

376 signals from ischemic macrophages synergize with the effects of hypoxia and nutrient

377 deprivation to induce a stronger EMT in tumor cells (Fig. 6D). Overall, we think that the

378 MEMIC provides a platform to model complex multicellular and heterogeneous *in vivo*

379 conditions. In addition to having most of the advantages of conventional *in vitro* cultures,

380 experiments in the MEMIC can be designed to incorporate high molecular and cellular

18

381   complexity. This complexity can be increased gradually to carefully tease apart key

382   factors shaping the tumor microenvironment. We believe that the process of

383   deconstructing tumors into their basic units, and then carefully reassembling them in the

384   MEMIC, will help us to better understand and control the tumor microenvironment.

385

MATERIALS AND METHODS

Cell culture

C6-HRE-GFP were a generous gift from Dr. Inna Serganova (Memorial Sloan Kettering

Cancer Center). PyMT cells were derived by Daniela Quail (McGill University). MDA-

MB-231 (HTB-26), HEK293T, and DLD-1 (CCL-221) cells were purchased from ATCC.

C6-HRE-GFP cells, MDA-MB-231 cells, DLD-1 cells, LN-99, and HEK293T cells were

grown in High Glucose DMEM (Gibco,11965-092) supplemented with 10% Fetal Bovine

Serum (FBS; Sigma-Aldrich, F0926). RPE cells were grown in High Glucose DMEM-

F12 medium (Gibco,11039) containing 10% FBS. All cells were incubated at 5% CO_2

and 37°C.

Animal protocols and differentiation of BMDMs

Bone marrow-derived macrophages (BMDMs) were extracted from C57BL/6 mice using

standard protocols (Gocheva et al., 2010). Following euthanization, femurs and tibiae

were harvested from both legs of the mice under sterile conditions. After careful

cleaning of the tissue, the bone marrow was flushed using a 25-gauge needle and

passed through a 40 μm strainer. The bone marrow flush was cultured in low

attachment culture dishes (VWR, 25384-342) in High Glucose DMEM supplemented

with 10% FBS, 10 ng/mL Recombinant Mouse CSF-1 (R&D Systems, 416-ML), and 1x

Antibiotic-Antimycotic (Gibco, 15240) for 7 days. Media was replaced every other day to

induce macrophage differentiation. All protocols involving animal work were approved

20

406   by NYU's University Animal Welfare Committee (UAWC protocols 17-1496 and 19-

407   1515).

Construction of genetic fluorescent reporters

409   To create a hypoxia reporter for live imaging, an existing GFP-based HIF1α reporter

410   (Vordermark et al., 2001), Addgene, 46926) was subcloned into a lentiviral delivery

411   plasmid using a Gibson assembly-based modular assembly platform (GMAP) (Akama-

412   Garren et al., 2016). The 5xHRE-GFP region and a PGK-driven puromycin selection

413   cassette from the pMSCV-Peredox-mCherry-NLS plasmid (Addgene, 32385) were

414   amplified using primers containing overhangs with the homology sites for GMAP cloning

415   and inserted into a lentiviral vector (LV 1-5, Addgene, 68411). This lentiviral backbone

416   was a gift from Dr. Tyler Jacks (Massachusetts Institute of Technology) and Dr. Thales

417   Papagiannakopoulos (New York University). The DNA construct for this new hypoxia

418   reporter is available in Addgene.

419   To create a fluorescent membrane label, we used the CAAX sequence method to target

420   a fluorescent protein to the plasma membrane (Hancock et al., 1989) . mCherry was

421   PCR amplified from pMSCV-Peredox-mCherry-NLS (Addgene, 32385) using primers

422   containing overhangs with the homology sites for GMAP cloning. The reverse primer

423   inserted the CAAX polybasic sequence. The CMV promoter and enhancer sequence to

424   drive CAAX-mCherry expression was amplified from pLenti-CMV-Puro-DEST plasmid

425   (Addgene, 17452). The two fragments were then assembled into one using overlapping

426   PCR and inserted into LV 1-5 using the GMAP method. The DNA construct for this new

21

427   fluorescent membrane reporter is available in Addgene.

428   Both resulting constructs were delivered to destination cells through lentiviral

429   transduction. Briefly, lentiviruses were packaged in HEK293T cells through co-

430   transfection with 2µg of VSV-G, 4µg of Delta8.9 viral vectors and 6µg of 5xHRE-GFP or

431   mCherry-CAAX vector using Lipofectamine 3000 reagent (Thermo Scientific, L3000) in

432   Opti-MEM (Gibco, 31985). The vectors mentioned above were kindly provided by Dr.

433   Nicholas P. Gauthier (Dana Farber Cancer Institute). On day 2, Opti-MEM media was

434   replaced with fresh DMEM supplemented with FBS. On days 3 and 5 after transfection,

435   the virus-containing medium was collected, filtered through 0.45µm filters, and

436   immediately stored at -80°C until infection. For lentiviral infection, 1mL of freshly thawed

437   virus media mixed with 1mL of culture media along with 10µg/mL polybrene was plated

438   onto destination cells in a 6-well plate at 40-60% confluency. For the 5xHRE-GFP

439   infection, infected cells were selected using 1µg/mL puromycin for 4 days starting 48

440   hours after transduction. For the mCherry-CAAX infection, infected cells were selected

441   using fluorescence-activated cell sorting. To create the cell line with both mCherry-

442   CAAX and 5xHRE-GFP, we used the lentiviral particles containing the mCherry-CAAX

443   insert to infect a 5xHRE-GFP cell line and then selected for using both selection

444   methods.

445   **Printing and Manufacturing the MEMIC**

446   The main framework of the MEMIC is 3D printed using fused filament fabrication, which

447   allows for on-demand supply as well as easy design modifications. For a detailed, step-

22

448   by-step MEMIC fabrication protocol, please refer to the supplementary information

449   attached to this manuscript and to supplementary videos S1 and S2. We designed the

450   framework using CAD software and printed them using Ultimaker 3D printers and black

451   PLA filament (Ultimaker) – a biocompatible, non-autofluorescent, and biodegradable

452   material. Other printers and other materials may be used as well, depending on printer

453   availability and experimental design. The printer settings, as well as the 3D design, that

454   we use can be found in the supplementary information of this paper. We showcase a

455   fused-filament-fabricated MEMIC version in this paper, as we believe that the

456   combination of the widening availability of fused filament printers in research facilities

457   and their precision would make this MEMIC the best option for most users. We also

458   describe other options in the supplementary information.

459   Once a 3D-printed framework was retrieved from the printer, glass coverslips (No. 1,

460   18x18 mm; VWR) were glued to it using a UV-curable adhesive (NOA68, Norland

461   Products) to create 12 individual chambers. We provide a detailed video on how to use

462   the NOA68 and how to glue coverslips onto the MEMIC (Video S2). To create the

463   bottom of the chambers, the coverslips were glued so that one completely covers each

464   opening. The glue must completely seal the glass surrounding the opening to prevent

465   leakage from the bottom of the chamber but should not seep into the surface of the

466   chamber where cells will be seeded, as this limits space for cell adhesion. Once the

467   adhesive was carefully applied, it was cured for 15 minutes under a long-wave UV lamp

468   (DR-5401, MelodySusie). To complete construction of the inner chamber, glass

469   coverslips were glued to the inside of each well with one edge against the inner ridge.

23

470   This created the top layer of the gradient chamber and an opening to the media

471   reservoir. Some chambers were left open without a top glass layer so that no gradients

472   form, which are used as controls. The top layer adhesive was cured for 15 minutes

473   under a long-wave UV lamp. For a fully detailed protocol on manufacturing and

474   illustrative images, please see the supplementary information.

475   To decouple the nutrient and hypoxia components of the ischemic gradient in the

476   MEMIC, in some experiments the glass coverslip was replaced with PDMS coverslips.

477   The PDMS coverslips were prepared using the Dow Sylgard 184 Silicone Encapsulant

478   Kit. To prepare PDMS coverslips, 1 part of the curing agent was thoroughly mixed with

479   10 parts of the silicone elastomer base by weight and centrifuged at 1300 RCF for 2-5

480   minutes to remove any air bubbles. A petri dish was then coated with about 6mL of the

481   mixture by gently swirling it. To remove trapped air bubbles, the dish was placed into a

482   vacuum desiccator for approximately 5 minutes. Curing was done by placing the PDMS

483   coated dish into an oven at 75ºC for at least 2 hours. The layer of PDMS was then cut

484   into 18x18mm squares, matching the dimensions of the glass coverslip. Since PDMS is

485   hydrophobic and may pose problems while gluing to the MEMIC framework, the PDMS

486   coverslips were treated with a plasma gun. Then, the PDMS coverslips were glued with

487   NOA68 optical adhesive as described for the top glass coverslips above.

488   **Seeding cells into the MEMIC**

489   To prepare the MEMIC for cell culture, the framework was first sterilized in a short-wave

490   UV lamp (CM-2009, Meishida). Then, the inner chambers and wells of the MEMIC were

491   washed twice with sterile DPBS (Gibco, 14040117). To improve cell attachment, the

24

492   chambers were filled with a 50µg/mL solution of Poly-D-Lysine (Sigma-Aldrich, P6407)

493   in DPBS and incubated at 37°C overnight, then washed twice with DPBS. Afterwards,

494   the chambers were washed with culture media. Cells to be seeded were detached from

495   their dish using 0.05% Trypsin-EDTA (Gibco, 25300-062). A cell suspension containing

496   10^6 cells/mL was prepared and the chambers were filled with 100µL of the suspension.

497   To open wells serving as controls, 500µL of the cell suspension and 2.5mL fresh media

498   was added. As the glass portion occupies about a fifth of the total surface of the well

499   bottom, the resulting cell density on the glass portion should be similar to the closed

500   wells. To allow cell attachment, the framework was placed into an incubator for

501   approximately an hour. Once cells settled to the bottom of the chamber, the reservoir of

502   the closed chambers was filled with 3mL fresh media. The framework was placed back

503   into the incubator to start gradient formation.

504   **Immunofluorescence**

505   After 24 hours of gradient formation, the media was aspirated from the wells and then

506   carefully aspirated from the chambers using a pipette to prevent cell loss. The cells

507   were fixed by filling the chambers with 2% (v/v) paraformaldehyde solution, obtained by

508   diluting 4% paraformaldehyde (Affymetrix, 19943) 1:1 in PBS (Fisher Scientific, BP399)

509   and incubating at room temperature for 5 minutes. The chambers were then gently

510   washed twice with PBS. To permeabilize the cells for staining, the chambers were filled

511   with a 0.1% (v/v) solution of Triton-X (Sigma-Aldrich, T8787) in PBS and incubated at

512   room temperature for 5 minutes. The chambers were gently washed twice with PBS and

513   filled with 100µL of blocking solution - 2.5% (w/v) bovine serum albumin (Sigma-Aldrich,

25

514   A9418) in PBS - and incubated for 1 hour at room temperature. The chambers were

515   gently washed twice with PBS. A primary antibody dilution was prepared in the blocking

516   solution with the antibodies diluted 1:200 for HIF1α (BD Bioscience, 610958), 1:50 for

517   phosphor-S6 (CST, 2211), 1:200 for E-cadherin (BD Bioscience, 610182), 1:200 for

518   phospho-H3 (CST, 3377), and 1:200 for CD68 (Serotec, MCA1957) and was added to

519   the chambers. The framework was placed inside a humidified chamber at 4°C. The

520   primary antibody solution was removed. The chambers were washed 3 times with PBS

521   and incubated at room temperature for 5 minutes. The chambers were then filled with a

522   secondary antibody (1:500 dilution) and nuclear stain solution (Hoechst 33342, 1:2000)

523   and incubated at room temperature for 1 hour in the dark. The chambers were finally

524   washed with PBS three times. To preserve cells until imaging, we filled the chambers

525   with a 0.02% (w/v) solution of sodium azide (Sigma-Aldrich, S2002) in PBS.

526   **Microscopy**

527   We imaged MEMICs using an inverted fluorescent microscope (Eclipse Ti2-E, Nikon)

528   equipped with a spinning disk confocal unit (X-Light V2, CrestOptics). For live imaging,

529   we used a stage top incubator (Tokai Hit, INUCG2-KRi) fed with a mixed gas source

530   (5% CO_2 in compressed air, Airgas, X02AI95C2000117). Entire chambers were imaged

531   in different fluorescent channels using tiling microscopy and then exported as stitched

532   16-bit TIF files.

533   **Image Cytometry Analysis**

534   Microscopy images were processed using our MATLAB-based scripts. A full tutorial on

26

535   how to use our image cytometry code for users without image analysis experience is

536   available with this paper (see SI for further details). This analytic approach can be used

537   with MEMIC images, and also with any other fluorescent images of cells or cell clusters

538   where fluorescence intensity and/or spatial information are of interest. Briefly, the

539   software intakes images of multiple replicates or conditions, with a single TIFF image

540   per channel per chamber, and outputs data on per cell fluorescence intensity, cell area

541   on the image, and cell position on the image. It also produces plots of fluorescence

542   intensity *versus* distance for each channel. The image analysis process requires that at

543   least one channel displays a uniform stain across, such as a nuclear stain for a cell

544   monolayer.

ACKNOWLEDGEMENTS

ADDITIONAL INFORMATION

553   Supplementary information is available for this paper. Please visit

554   http://carmofon.org/publications/newmemic/ to download updated designs of the MEMIC

555   and other information relevant to this work. Correspondence and requests for materials

27
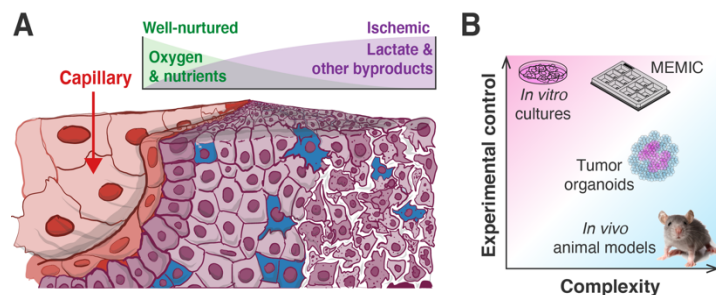
556   should be addressed to C.C.-F.

FIGURE LEGENDS

Figure 1: The complexity of the tumor microenvironment and its experimental models.

A. Due to the poor vascularization tumor cells are exposed to different metabolic conditions according to their distance to blood vessels. Proximal cells readily obtain oxygen and nutrients, while distal cells endure a lack of resources and accumulation of metabolic byproducts.
B. Models of the tumor microenvironment. *In vitro* cultures provide a high level of experimental control but they cannot capture key features of the tumor microenvironment. The complexity of *in vivo* models – and to some extent of 3D organoid cultures – comes at the cost of experimental control. The MEMIC allows for high complexity *in vitro* and *ex vivo* cultures while allowing for full experimental control.
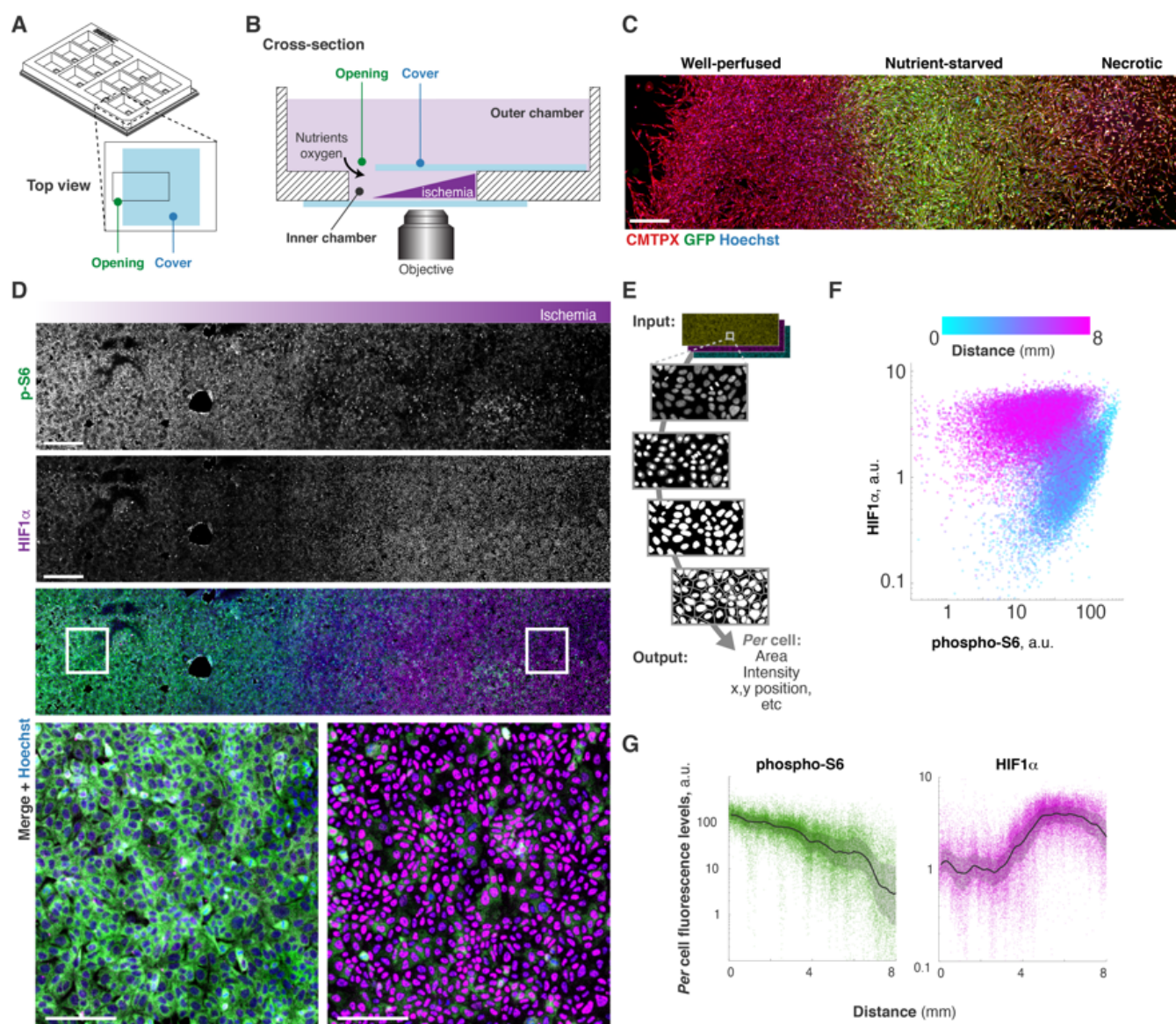
Figure 2: Formation of metabolic gradients in the MEMIC

A. View of 3D-printed framework containing 12 independent MEMICs. Each chamber is located within a separate well.

B. Cross-section view of a MEMIC. Cells are cultured in the inner chamber, generating metabolic gradients. The chamber is enclosed by a top and bottom glass coverslip, except for a narrow opening to a media reservoir, allowing for unilateral diffusion of fresh media into the chamber.

C. Cells expressing a of a GFP-based hypoxia after 24h culture in the MEMIC. Cells show distinct metabolic landscapes. Scale bar: 500μm.

D. Metabolic conditions affect cell signaling and transcriptional programs. Immunofluorescent staining of DLD1 cells for phosphorylated ribosomal protein S6 (p-S6, a readout of active mTOR signaling, green) and for the transcription factor Hif1α (purple). Scale bars: 800μm, 200μm for insets.

E. A typical image cytometry pipeline.

F. Quantification of **D.** shows p-S6 and Hif1α levels *per* cell. Note the two distinct populations determined by the distance from the opening of the MEMIC.

G. Quantification of **D.** shows opposite trends in intensity of p-S6 and Hif1α. Lines: moving median values, shaded region: interquartile range.
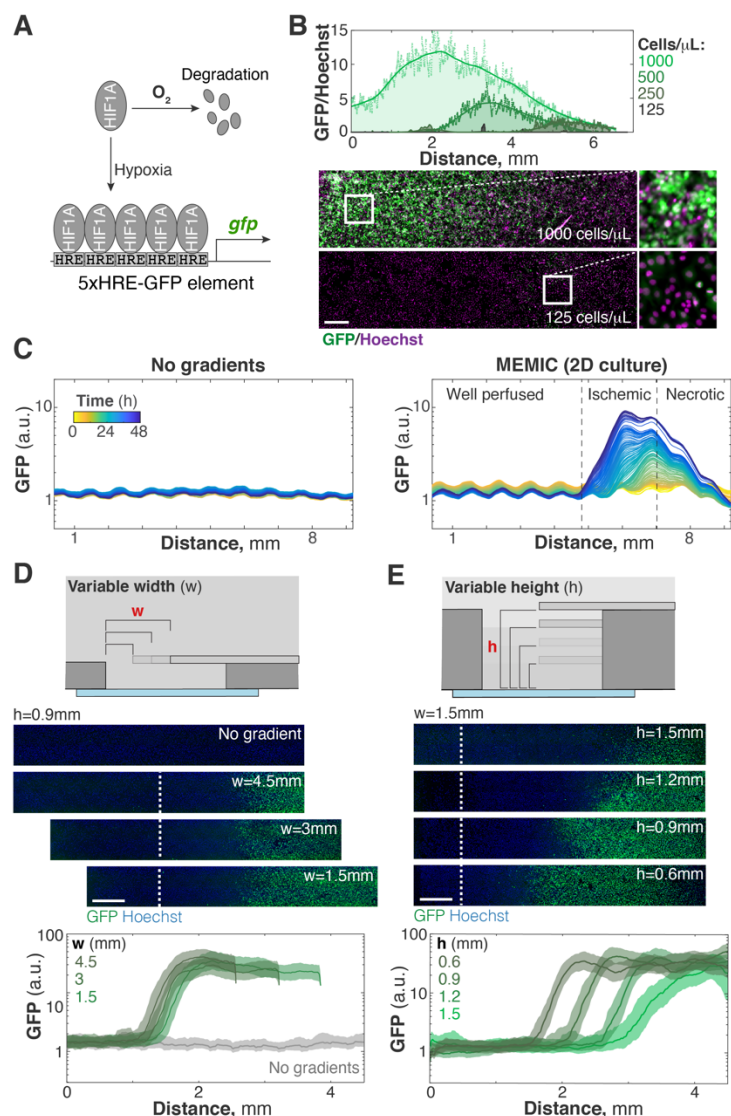
30

Figure 3: Key parameters in shaping metabolic gradients in the MEMIC

A. We used a GFP-based hypoxia reporter (5xHRE-GFP) as a readout for resource limitation.

B. Cell density has a dramatic effect in the shape of metabolic gradients. Top: median GFP levels (normalized by Hoechst) for MDA-MB-231 cells expressing 5xHRE-GFP and cultured at different densities for 24hr in the MEMIC. Bottom: Representative images of highest and lowest densities. Scale bar: 200µm.

C. Monolayer of 5HRE-GFP MDA-MB-231 cells shows that gradient formation in the MEMIC is dynamic and time dependent. Lines: moving median GFP intensity, color-coded by time.

D. 5HRE-GFP MDA-MB-231 cells form gradients at the same distance from the opening and with the same shape when the width of the MEMIC opening is changed. Lines: moving median GFP intensity, shaded regions: interquartile range.

E. 5HRE-GFP MDA-MB-231 cells form gradients that are further from the opening and shallower the taller the MEMIC chamber. Lines: moving median GFP intensity, shaded regions: interquartile range. Scale bars for C and D: 500µm.
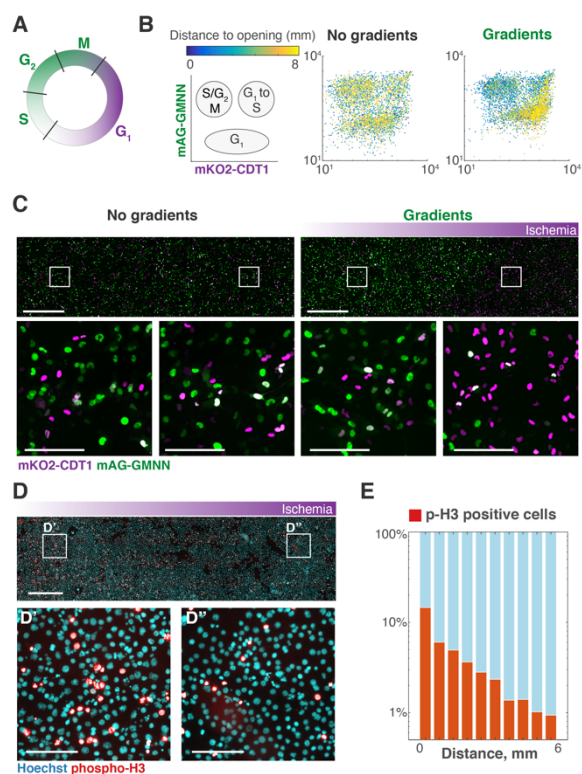
Figure 4: Gradients of ischemia induce spatial patterns of cell proliferation

A. Relationship between mKO2-CDT1 (purple) and mAG-GMNN (green) fluorescent levels and cell cycle phases for cells expressing FUCCI.

B. Quantification of FUCCI fluorescence RPE1 cells intensity in each cell nuclei. Cells arrested in G1 are much more abundant in ischemic regions.

C. Representative images of RPE1 cells expressing FUCCI culture without gradients or in the MEMIC. Scale bars: 1000μm, insets: 200μm.

D. Immunofluorescent staining of phospho-H3 (red) in DLD1 tumor cells cultured in the MEMIC. Scale bars: 1000μm, insets: 100μm.

E. Quantification of **D.** shows the percentage of phospho-H3 positive cells binned along the distance from the opening. The percentage of proliferating cells drops in ischemic regions.
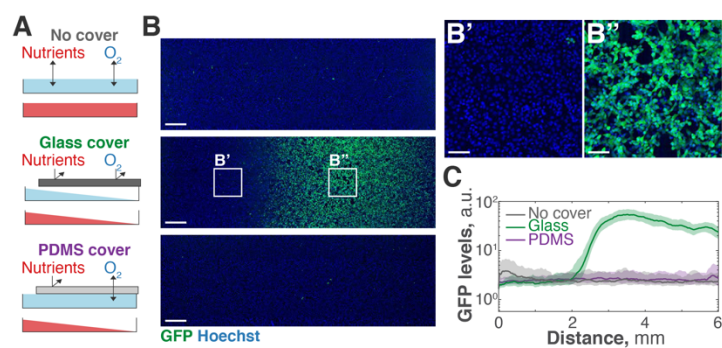
Figure 5: Untangling gradients of hypoxia from other metabolites

A. Schematic showing the different experimental conditions depending on the use of glass or PDMS coverslips in the MEMIC. PDMS is permeable to gases, but not soluble metabolites, decoupling the nutrient gradients from hypoxia.

B. 5HRE-GFP MDA-MB-231 cells grown in the MEMIC show hypoxia (GFP) in MEMIC with glass but not with PDMS coverslips (detail in **B'** and **B''**). Scale bars: 500µm, 100µm for insets.

C. Quantification of GFP levels for all three conditions. Lines: moving medians, shaded regions: interquartile range.
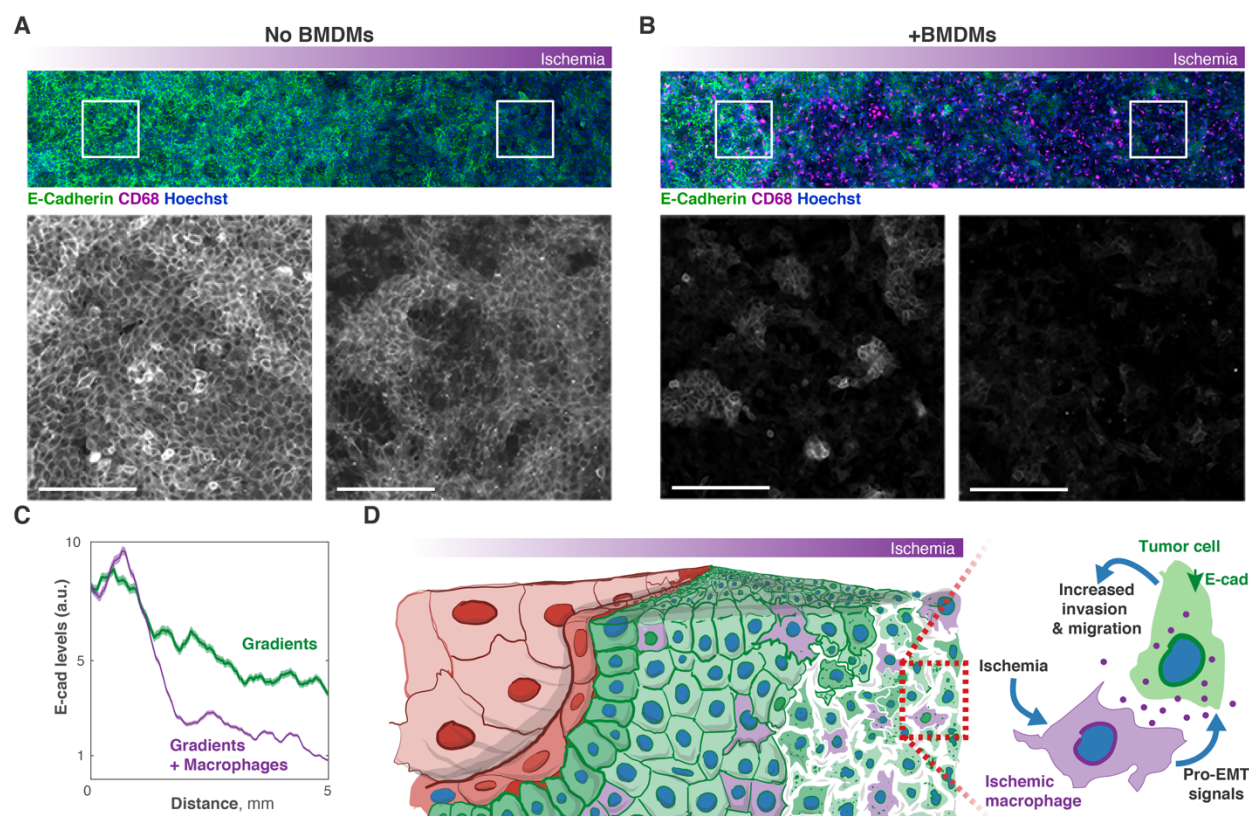
Figure 6: Non-cell autonomous effects of ischemia

A. Cells derived from MMTV-PyMT breast tumors decrease E-Cadherin expression (green) in ischemic areas of the MEMIC. Scale bars: 200µm.

B. Cells derived from MMTV-PyMT breast tumors co-cultured with bone-marrow-derived macrophages (CD68 immunofluorescence, magenta) show a stronger decrease in E-cadherin levels. Scale bars: 200µm.

C. Quantification of **A.** and **B.** shows that the presence of macrophages synergizes with ischemic conditions to suppress E-cadherin expression. Lines: moving medians, shaded regions: interquartile range.

D. Schematic showing how multiple factors within the tumor microenvironment synergize to promote EMT in tumor cells. Ischemic conditions induce EMT markers in tumor cells, which ischemic macrophages boost further.

REFERENCES

Akama-Garren, E. H., Joshi, N. S., Tammela, T., Chang, G. P., Wagner, B. L., Lee, D.-Y., Rideout, W. M., Papagiannakopoulos, T., Xue, W. and Jacks, T. (2016). A Modular Assembly Platform for Rapid Generation of DNA Constructs. *Scientific Reports* **6**, 16836.

Bader, J. E., Voss, K. and Rathmell, J. C. (2020). Targeting Metabolism to Improve the Tumor Microenvironment for Cancer Immunotherapy. *Mol Cell* **78**, 1019–1033.

Baish, J. W. and Jain, R. K. (2000). Fractals and cancer. *Cancer Res* **60**, 3683–8.

Bert, B., Dörendahl, A., Leich, N., Vietze, J., Steinfath, M., Chmielewska, J., Hensel, A., Grune, B. and Schönfelder, G. (2017). Rethinking 3R strategies: Digging deeper into AnimalTestInfo promotes transparency in in vivo biomedical research. *Plos Biol* **15**, e2003217.

Birsoy, K., Wang, T., Chen, W. W., Freinkman, E., Abu-Remaileh, M. and Sabatini, D. M. (2015). An Essential Role of the Mitochondrial Electron Transport Chain in Cell Proliferation Is to Enable Aspartate Synthesis. *Cell* **162**, 540–551.

Boj, S. F., Hwang, C.-I., Baker, L. A., Chio, I. I. C., Engle, D. D., Corbo, V., Jager, M., Ponz-Sarvise, M., Tiriac, H., Spector, M. S., et al. (2015). Organoid Models of Human and Mouse Ductal Pancreatic Cancer. *Cell* **160**, 324–338.

Bose, S., Allen, A. E. and Locasale, J. W. (2020). The Molecular Link from Diet to Cancer Cell Metabolism. *Mol Cell* **78**, 1034–1044.

Bressers, S., Elzen, H. van den, Gräwe, C., Oetelaar, D. van den, Postma, P. H. A. and Schoustra, S. K. (2019). Policy driven changes in animal research practices: mapping researchers' attitudes towards animal-free innovations using the Netherlands as an example. *Res Integr Peer Rev* **4**, 8.

Buck, M. D., Sowell, R. T., Kaech, S. M. and Pearce, E. L. (2017). Metabolic Instruction of Immunity. *Cell* **169**, 570–586.

Carmeliet, P. and Jain, R. K. (2000a). Angiogenesis in cancer and other diseases. *Nature* **407**, 249–257.

Carmeliet, P. and Jain, R. K. (2000b). Angiogenesis in cancer and other diseases. *Nature* **407**, 249–257.

Carmona-Fontaine, C., Bucci, V., Akkari, L., Deforet, M., Joyce, J. A. and Xavier, J. B. (2013). Emergence of spatial structure in the tumor microenvironment due to the Warburg effect. *Proceedings of the National Academy of Sciences* **110**, 19402–19407.

Carmona-Fontaine, C., Deforet, M., Akkari, L., Thompson, C. B., Joyce, J. A. and Xavier, J. B. (2017a). Metabolic origins of spatial organization in the tumor microenvironment. *Proceedings of the National Academy of Sciences* **114**, 2934–2939.

Carmona-Fontaine, C., Deforet, M., Akkari, L., Thompson, C. B., Joyce, J. A. and Xavier, J. B. (2017b). Metabolic origins of spatial organization in the tumor microenvironment. *Proceedings of the National Academy of Sciences* **114**, 2934–2939.

Clevers, H. (2016). Modeling Development and Disease with Organoids. *Cell* **165**, 1586–1597.

Colegio, O. R., Chu, N.-Q., Szabo, A. L., Chu, T., Rhebergen, A. M., Jairam, V., Cyrus, N., Brokowski, C. E., Eisenbarth, S. C., Phillips, G. M., et al. (2014). Functional polarization of tumour-associated macrophages by tumour-derived lactic acid. *Nature* **513**, 559–563.

Condeelis, J. and Pollard, J. W. (2006). Macrophages: Obligate Partners for Tumor Cell Migration, Invasion, and Metastasis. *Cell* **124**, 263–266.

Cox, M. E. and Dunn, B. (1986). Oxygen diffusion in poly(dimethyl siloxane) using fluorescence quenching. I. Measurement technique and analysis. *J Polym Sci Part Polym Chem* **24**, 621–636.

Davoli, T. and Lange, T. de (2011). The Causes and Consequences of Polyploidy in Normal Development and Cancer. *Annu Rev Cell Dev Bi* **27**, 585–610.

Day, C.-P., Merlino, G. and Dyke, T. V. (2015). Preclinical mouse cancer models: a maze of opportunities and challenges. *Cell* **163**, 39–53.

Dongre, A. and Weinberg, R. A. (2018). New insights into the mechanisms of epithelial–mesenchymal transition and implications for cancer. *Nat Rev Mol Cell Bio* **20**, 69–84.

Ducker, G. S. and Rabinowitz, J. D. (2016). One-Carbon Metabolism in Health and Disease. *Cell Metab* **25**, 27–42.

Gao, D., Vela, I., Sboner, A., Iaquinta, P. J., Karthaus, W. R., Gopalan, A., Dowling, C., Wanjala, J. N., Undvall, E. A., Arora, V. K., et al. (2014). Organoid Cultures Derived from Patients with Advanced Prostate Cancer. *Cell* **159**, 176–187.

Gatenby, R. A. and Gillies, R. J. (2004). Why do cancers have high aerobic glycolysis? *Nat Rev Cancer* **4**, 891–899.

Gatenby, R. A. and Gillies, R. J. (2008). A microenvironmental model of carcinogenesis. *Nat Rev Cancer* **8**, 56–61.

Gocheva, V., Wang, H.-W., Gadea, B. B., Shree, T., Hunter, K. E., Garfall, A. L., Berman, T. and Joyce, J. A. (2010). IL-4 induces cathepsin protease activity in tumor-associated macrophages to promote cancer growth and invasion. *Gene Dev* **24**, 241–255.

Gordon, R. R. and Nelson, P. S. (2012). Cellular senescence and cancer chemotherapy resistance. *Drug Resist Update* **15**, 123–131.

Gould, S. E., Junttila, M. R. and Sauvage, F. J. de (2015). Translational value of mouse models in oncology drug development. *Nat Med* **21**, 431–9.

Halbrook, C. J., Thurston, G., McCarthy, A., Nelson, B. S., Sajjakulnukit, P., Krall, A. S., Mullen, P. J., Zhang, L., Batra, S., Viale, A., et al. (2020). Clonal Heterogeneity Supports Mitochondrial Metabolism in Pancreatic Cancer. *Biorxiv* 2020.05.15.098368.

Hancock, J. F., Magee, A. I., Childs, J. E. and Marshall, C. J. (1989). All ras proteins are polyisoprenylated but only some are palmitoylated. *Cell* **57**, 1167–1177.

Heiden, M. G. V., Cantley, L. C. and Thompson, C. B. (2009). Understanding the Warburg effect: the metabolic requirements of cell proliferation. *Sci New York N Y* **324**, 1029–33.

Hobson-Gutierrez, S. A. and Carmona-Fontaine, C. (2018a). The metabolic axis of macrophage and immune cell polarization. *Dis Model Mech* **11**, dmm034462.

Hobson-Gutierrez, S. A. and Carmona-Fontaine, C. (2018b). The metabolic axis of macrophage and immune cell polarization. *Dis Model Mech* **11**, dmm034462.

Jain, M., Nilsson, R., Sharma, S., Madhusudhan, N., Kitami, T., Souza, A. L., Kafri, R., Kirschner, M. W., Clish, C. B. and Mootha, V. K. (2012). Metabolite Profiling Identifies a Key Role for Glycine in Rapid Cancer Cell Proliferation. *Science* **336**, 1040–1044.

Junttila, M. R. and Sauvage, F. J. de (2013). Influence of tumour micro-environment heterogeneity on therapeutic response. *Nature* **501**, 346–354.

Krall, A. S., Mullen, P. J., Surjono, F., Momcilovic, M., Schmid, E. W., Halbrook, C. J., Thambundit, A., Mittelman, S. D., Lyssiotis, C. A., Shackelford, D. B., et al. (2020). Asparagine signals mitochondrial respiration and can be targeted to impair tumour growth. *Biorxiv* 2020.03.17.995670.

Lee, D. C., Sohn, H. A., Park, Z.-Y., Oh, S., Kang, Y. K., Lee, K.-M., Kang, M., Jang, Y. J., Yang, S.-J., Hong, Y. K., et al. (2015). A lactate-induced response to hypoxia. *Cell* **161**, 595–609.

Linde, N., Casanova-Acebes, M., Sosa, M. S., Mortha, A., Rahman, A., Farias, E., Harper, K., Tardio, E., Torres, I. R., Jones, J., et al. (2018). Macrophages orchestrate breast cancer early dissemination and metastasis. *Nat Commun* **9**, 21.

Lyssiotis, C. A. and Kimmelman, A. C. (2017). Metabolic Interactions in the Tumor Microenvironment. *Trends Cell Biol* **27**, 863–875.

Maddocks, O. D. K., Berkers, C. R., Mason, S. M., Zheng, L., Blyth, K., Gottlieb, E. and Vousden, K. H. (2012). Serine starvation induces stress and p53-dependent metabolic remodelling in cancer cells. *Nature* **493**, 542–546.

Mazzone, M., Dettori, D., Oliveira, R. L. de, Loges, S., Schmidt, T., Jonckx, B., Tian, Y.-M., Lanahan, A. A., Pollard, P., Almodovar, C. R. de, et al. (2009). Heterozygous Deficiency of PHD2 Restores Tumor Oxygenation and Inhibits Metastasis via Endothelial Normalization. *Cell* **136**, 839–851.

Mehta, M. M., Weinberg, S. E. and Chandel, N. S. (2017). Mitochondrial control of immunity: beyond ATP. *Nat Rev Immunol* **17**, 608–620.

Merlo, L. M. F., Pepper, J. W., Reid, B. J. and Maley, C. C. (2006). Cancer as an evolutionary and ecological process. *Nat Rev Cancer* **6**, 924–935.

Nieto, M. A. (2013). Epithelial Plasticity: A Common Theme in Embryonic and Cancer Cells. *Science* **342**, 1234850–1234850.

Olenchock, B. A., Rathmell, J. C. and Heiden, M. G. V. (2017a). Biochemical Underpinnings of Immune Cell Metabolic Phenotypes. *Immunity* **46**, 703–713.

Olenchock, B. A., Rathmell, J. C. and Heiden, M. G. V. (2017b). Biochemical Underpinnings of Immune Cell Metabolic Phenotypes. *Immunity* **46**, 703–713.

Oshima, K., Zhao, J., Pérez-Durán, P., Brown, J. A., Patiño-Galindo, J. A., Chu, T., Quinn, A., Gunning, T., Belver, L., Ambesi-Impiombato, A., et al. (2020). Mutational and functional genetics mapping of chemotherapy resistance mechanisms in relapsed acute lymphoblastic leukemia. *Nat Cancer* **1**, 1113–1127.

Palm, W., Park, Y., Wright, K., Pavlova, N. N., Tuveson, D. A. and Thompson, C. B. (2015). The Utilization of Extracellular Proteins as Nutrients Is Suppressed by mTORC1. *Cell* **162**, 259–270.

Pavlova, N. N. and Thompson, C. B. (2016a). The Emerging Hallmarks of Cancer Metabolism. *Cell Metab* **23**, 27–47.

Pavlova, N. N. and Thompson, C. B. (2016b). The Emerging Hallmarks of Cancer Metabolism. *Cell Metabolism* **23**, 27–47.

Pavlova, N. N., Hui, S., Ghergurovich, J. M., Fan, J., Intlekofer, A. M., White, R. M., Rabinowitz, J. D., Thompson, C. B. and Zhang, J. (2018). As Extracellular Glutamine Levels Decline, Asparagine Becomes an Essential Amino Acid. *Cell Metab* **27**, 428-438.e5.

Possemato, R., Marks, K. M., Shaul, Y. D., Pacold, M. E., Kim, D., Birsoy, K., Sethumadhavan, S., Woo, H.-K., Jang, H. G., Jha, A. K., et al. (2011). Functional genomics reveal that the serine synthesis pathway is essential in breast cancer. *Nature* **476**, 346–350.

Sakaue-Sawano, A., Kurokawa, H., Morimura, T., Hanyu, A., Hama, H., Osawa, H., Kashiwagi, S., Fukami, K., Miyata, T., Miyoshi, H., et al. (2008). Visualizing Spatiotemporal Dynamics of Multicellular Cell-Cycle Progression. *Cell* **132**, 487–498.

Saxton, R. A. and Sabatini, D. M. (2017). mTOR Signaling in Growth, Metabolism, and Disease. *Cell* **169**, 361–371.

Son, J., Lyssiotis, C. A., Ying, H., Wang, X., Hua, S., Ligorio, M., Perera, R. M., Ferrone, C. R., Mullarky, E., Shyh-Chang, N., et al. (2013). Glutamine supports pancreatic cancer growth through a KRAS-regulated metabolic pathway. *Nature* **496**, 101–5.

Sullivan, L. B., Gui, D. Y., Hosios, A. M., Bush, L. N., Freinkman, E. and Vander Heiden, M. G. (2015). Supporting Aspartate Biosynthesis Is an Essential Function of Respiration in Proliferating Cells. *Cell* **162**, 552–563.

Tabassum, D. P. and Polyak, K. (2015). Tumorigenesis: it takes a village. *Nat Rev Cancer* **15**, 473–483.

Thomlinson, R. H. (1977a). Hypoxia and tumours. *J Clin Pathol* **s3-11**, 105.

Thomlinson, R. H. (1977b). Hypoxia and tumours. *Journal of clinical pathology* **11**, 105–113.

van de Wetering, M., Francies, H. E., Francis, J. M., Bounova, G., Iorio, F., Pronk, A., van Houdt, W., van Gorp, J., Taylor-Weiner, A., Kester, L., et al. (2015). Prospective Derivation of a Living Organoid Biobank of Colorectal Cancer Patients. *Cell* **161**, 933–945.

Vordermark, D., Shibata, T. and Brown, J. M. (2001). Green fluorescent protein is a suitable reporter of tumor hypoxia despite an oxygen requirement for chromophore formation. *Neoplasia (New York, N.Y.)* **3**, 527–534.

Watkins, T. B. K., Lim, E. L., Petkovic, M., Elizalde, S., Birkbak, N. J., Wilson, G. A., Moore, D. A., Grönroos, E., Rowan, A., Dewhurst, S. M., et al. (2020). Pervasive chromosomal instability and karyotype order in tumour evolution. *Nature* 1–7.

Weinberg, R. A. (2013). The Biology of Cancer.

Wenes, M., Shang, M., Di Matteo, M., Goveia, J., Martín-Pérez, R., Serneels, J., Prenen, H., Ghesquière, B., Carmeliet, P. and Mazzone, M. (2016). Macrophage Metabolism Controls Tumor Blood Vessel Morphogenesis and Metastasis. *Cell Metab* **24**, 701–715.

Wiseman, H. and Halliwell, B. (1996). Damage to DNA by reactive oxygen and nitrogen species: Role in inflammatory disease and progression to cancer. *Biochemical Journal* **313**, 17–29.

Wong, C. C.-L., Gilkes, D. M., Zhang, H., Chen, J., Wei, H., Chaturvedi, P., Fraley, S. I., Wong, C.-M., Khoo, U.-S., Ng, I. O.-L., et al. (2011). Hypoxia-inducible factor 1 is a master regulator of breast cancer metastatic niche formation. *P Natl Acad Sci Usa* **108**, 16369–74.

Yano, S., Zhang, Y., Miwa, S., Tome, Y., Hiroshima, Y., Uehara, F., Yamamoto, M., Suetsugu, A., Kishimoto, H., Tazawa, H., et al. (2014). Spatial-temporal FUCCI imaging of each cell in a tumor demonstrates locational dependence of cell cycle dynamics and chemoresponsiveness. *Cell Cycle* **13**, 2110–2119.

Zhong, H., Marzo, A. M. D., Laughner, E., Lim, M., Hilton, D. A., Zagzag, D., Buechler, P., Isaacs, W. B., Semenza, G. L. and Simons, J. W. (1999). Overexpression of hypoxia-inducible factor 1alpha in common human cancers and their metastases. *Cancer Res* **59**, 5830–5.